

OPEN

Thickness-induced metal to insulator transition in Ru nanosheets probed by photoemission spectroscopy: Effects of disorder and Coulomb interaction

Daiki Ootsuki^{1*}, Kenjiro Kodera¹, Daiya Shimonaka¹, Masashi Arita², Hirofumi Namatame², Masaki Taniguchi², Makoto Minohara³, Koji Horiba³, Hiroshi Kumigashira³, Eiji Ikenaga⁴, Akira Yasui⁴, Yoshiharu Uchimoto¹, Satoshi Toyoda⁵, Masahito Morita⁶, Katsutoshi Fukuda⁶ & Teppei Yoshida^{1*}

We investigated the electronic structures of mono- and few-layered Ru nanosheets (N layers (L)) with $N=1$, ~ 6 , and ~ 9) on Si substrate by ultra-violet and x-ray photoemission spectroscopies. The spectral density of states (DOS) near E_F of ~ 6 L and 1 L is suppressed as it approaches E_F in contrast to that of ~ 9 L, which is consistent with the Ru 3 d core-level shift indicating the reduction of the metallic conductivity. A power law $g(\varepsilon) \propto |\varepsilon - \varepsilon_F|^\alpha$ well reproduces the observed spectral DOS of ~ 6 L and 1 L. The evolution of the power factor α suggests that the transition from the metallic state of ~ 9 L to the 2-dimensional insulating state with the soft Coulomb gap of 1 L through the disordered 3-dimensional metallic state of ~ 6 L.

The discovery of 2-dimensional crystal composed of a carbon monolayer, so called graphene, has evoked much attention to the physical properties in the atomic layer limit as well as applied researches for the electronic and photonic devices¹. What is interesting about atomic layer crystals such as graphene, silicene, germanene, and stanene is the different physical properties from the bulk nature¹⁻⁶. Recently, 2-dimensional material Ru nanosheet consisting of a single element Ruthenium was successfully synthesized by topotactic reaction method⁷. The schematics of the mono- and few layered Ru nanosheets are displayed in Fig. 1. The optical absorption spectra of Ru nanosheets highly depend on the number of layers, indicating the disappearance of the metallic conductivity in mono-layered (1 L) and bi-layered Ru nanosheets (2 L)⁸. Toyoda *et al.* suggested that the ligand-driven covalency and the metallicity abruptly occur between bilayer (2 L) and trilayer (3 L) Ru nanosheets⁹. Controlling the metallicity by the number of layers are promising applications associated with microelectronics. However, the mechanism responsible for the non-metallic behavior in the mono-layered Ru nanosheets is unknown.

In this work, we investigated how the electronic structure evolves from the mono- (1 L) to few layered Ru nanosheets ~ 6 and ~ 9 L on Si substrate by performing photoemission spectroscopy in order to clarify the mechanism of the disappearance of the metallic conductivity. We observed the chemical shifts of Ru 3 d core-level spectra and the suppression of the spectral weight at Fermi-level (E_F) with decreasing the number of stacking layers.

¹Graduate School of Human and Environmental Studies, Kyoto University, Sakyo-ku, Kyoto, 606-8501, Japan.

²Hiroshima Synchrotron Radiation Center, Hiroshima University, Higashi-hiroshima, 739-0046, Japan. ³Institute of Materials Structure Science, High Energy Accelerator Research Organization (KEK), Tsukuba, Ibaraki, 305-0801, Japan. ⁴SPring-8/JASRI, 1-1-1 Koto, Sayo-cho, Hyogo, 679-5198, Japan. ⁵Department of Materials Science and Engineering, Kyoto University, Sakyo-ku, Kyoto, 606-8501, Japan. ⁶Office of Society-Academia Collaboration for Innovation, Kyoto University, Sakyo-ku, Kyoto, 606-8501, Japan. *email: ootsuki.daiki.4z@kyoto-u.ac.jp; yoshida.teppei.8v@kyoto-u.ac.jp

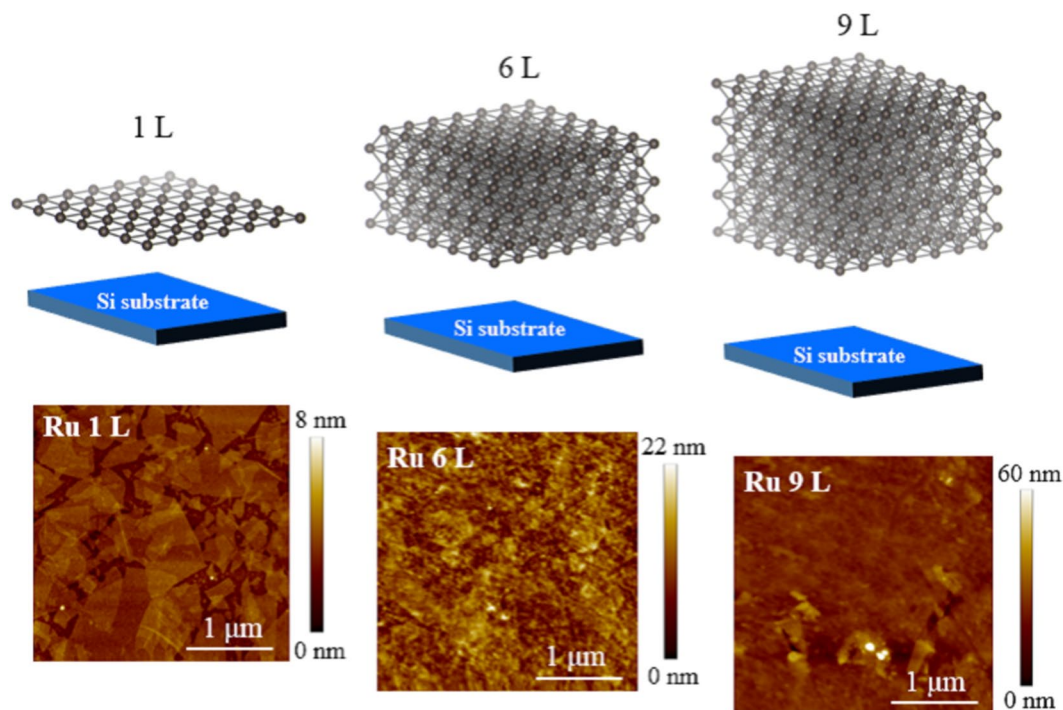


Figure 1. Schematics and AFM images of Ru nanosheets (1, 6, and 9 L).

These indicate the disappearance of the metallic conductivity in the mono-layered Ru nanosheets. Moreover, we reproduced the spectral weight near E_F using a power law $g(\varepsilon) \propto |\varepsilon - \varepsilon_F|^\alpha$. The evolution of the power factor α suggests that the transition from the metallic state of ~ 9 L to the 2-dimensional insulating state with the soft Coulomb gap of 1 L through the disordered 3-dimensional metallic state of ~ 6 L.

Methods

Ru nanosheets were prepared following the previously described an electrostatic self-assembly method in Refs. ^{7,8}. A Si (111) wafer as substrate was cleaned by HCl-CH₃OH (1:1) solution and then by H₂SO₄ solution. The Si wafer was immersed in an aqueous solution of coblock polymer composed of polyvinyl alcohol and polyvinylamine for 20 min to coat the surface. It was then dipped in a colloidal suspension of negatively charged RuO₂ nanosheets. The number of layers N was controlled by repeating this cycle. The obtained RuO₂ nanosheets were reduced by the hydrogen reduction at 200 °C under the gas-flow-controlled condition (5% H₂ and 95% Ar, 250 mL/min) and the Ru nanosheets were fabricated. The Ru nanosheets are composed of the atomic mono-layered hexagonal system with the bond length of the first-nearest-neighbor atoms to be 2.74 Å for 1 L and 2.65 Å for ≥ 6 L⁷.

A tapping-mode atomic force microscopy (AFM; Innova, Bruker Inc.) was used to obtain Ru nanosheets images. The AFM images of the fabricated Ru nanosheets for 1 L, ~ 6 L, and ~ 9 L are displayed in Fig. 1. The AFM image of 1 L shows single-crystal arrays, overlapped patches, and a bare surface. The total coverage is estimated to be approximately 82.5% and the fraction of the overlapping region to be 33.7%. For the few-layered Ru nanosheets, the number of layers is basically determined by the cycles of the fabrication process used to prepared the RuO₂ nanosheets. In our fabrication process, the few-layered Ru nanosheets have variations of the number of layers. Assuming the thickness of 0.72 nm for 1 L from the difference between 1 L and the overlapped region (2L), we obtained the variations for ± 3.1 L for 6 L and ± 3.0 for 9 L, respectively. The large variations of the few-layered Ru nanosheets suggest the acceleration of crystallization and/or the existence of the stacking fault by large motion of atom.

Photoemission spectroscopy measurements were performed at BL47XU of SPring-8, BL2A of Photon Factory (PF), and BL9A of Hiroshima Synchrotron Radiation Center (HiSOR) equipped the VG-Scienta R4000 electron analyzer. The electron analyzers are placed at 90° for SPring-8 BL47XU, 40° for PF BL2A, and 50° for HiSOR BL9A to the incident beam. The incident angles relative to the sample surface are set to at 12° for SPring-8 BL47XU, 50° for PF BL2A, and 40° for HiSOR BL9A. Linearly polarized photon of the incident beam was used at all beam-lines. The beam sizes are about 40 μm \times 30 μm for SPring-8 BL47XU, 100 μm \times 1 m for PF BL2A, and 1.5 mm \times 1.0 mm² for HiSOR BL9A. The photoemission data were collected at $T = 300$ K for $h\nu = 7940$ eV at SPring-8 BL47XU, $T = 15$ K for $h\nu = 800$ eV at PF BL-2A, and $T = 28$ K for $h\nu = 20$ eV at HiSOR BL-9A, respectively. By fitting of the gold spectrum to the Fermi-Dirac function convoluted with the Gaussian function corresponding to the total-energy resolution, we obtained the total-energy resolutions of 265 meV for $h\nu = 7940$ eV, 203 meV for $h\nu = 800$ eV, and 19 meV for $h\nu = 20$ eV, respectively. The base pressures of the spectrometer for each beam-line were better than 1.0×10^{-10} Torr. The probability of a primary photoelectron escaping from the depth z is

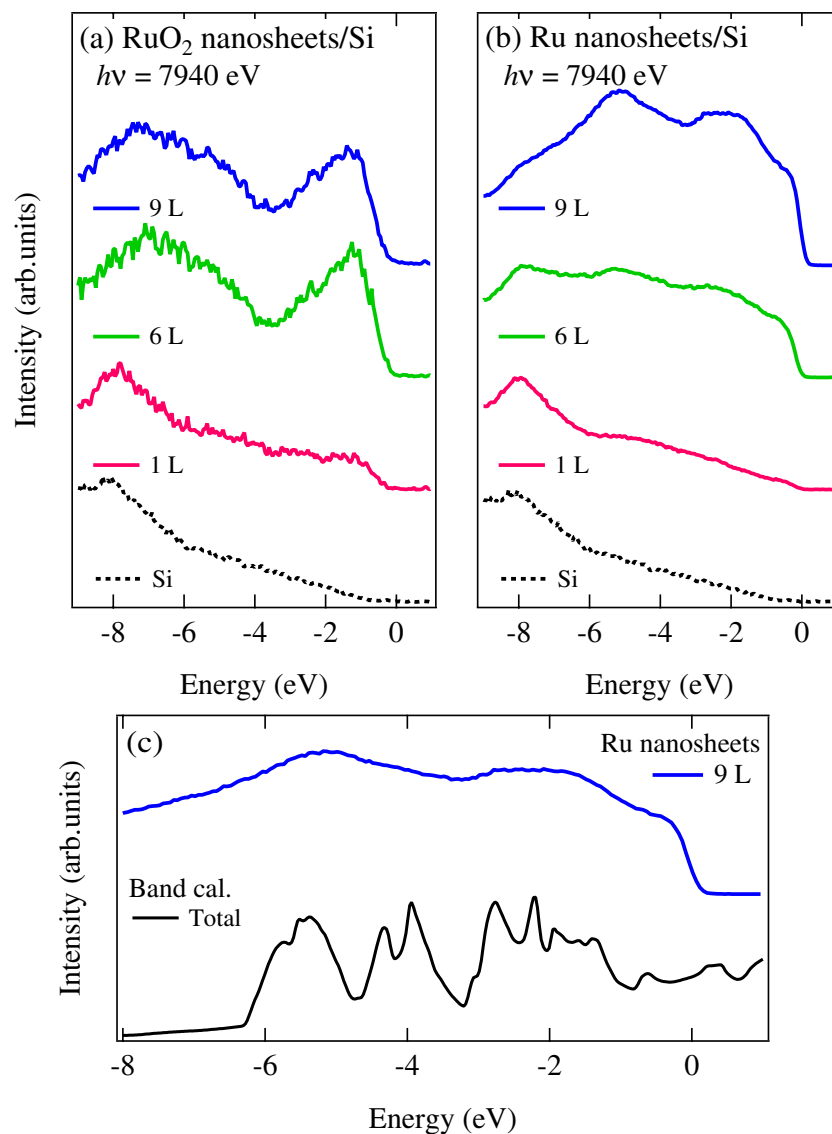


Figure 2. Valence-band photoemission spectra of (a) RuO₂ and (b) Ru nanosheets (1, ~6, and ~9 L) taken at $h\nu = 7940$ eV. The dotted curve shows the spectrum of Si substrate without RuO₂ and Ru nanosheets. (c) The valence band spectrum of the Ru nanosheets (~9 L) compared with the band structure calculation of bulk Ru metal. The data were collected at $T = 300$ K without surface treatment because of the large probing depth of hard x-ray. The spectra were normalized to the intensity around -8 eV.

proportional to $\exp(-z/\lambda)$ where λ is an inelastic scattering mean free path (IMFP) for electrons in solid. Here, λ is about 7.4 nm for $h\nu = 7940$ eV, 1.3 nm for $h\nu = 800$ eV, and 1.0 nm for $h\nu = 20$ eV estimated from refs. ^{10,11}.

The band structure calculation was carried out using the code WIEN2k¹⁰ based on the full-potential linearized augmented plane wave method. The calculated results were obtained the generalized gradient approximation for electron correlations, where we used the exchange-correlation potential¹¹. The spin-orbit interaction is not taken into account.

Results and Discussion

Figure 2(a,b) show the valence-band photoemission spectra of RuO₂ and Ru nanosheets (1, ~6, and ~9 L) on Si substrate. The dotted curve indicates the photoemission spectrum of Si substrate without RuO₂ or Ru nanosheets. The intensity from the Si substrate as well as that from the nanosheets is certainly observed in RuO₂ and Ru nanosheets, because of the large IMFP λ of 7.44 nm for the hard x-ray photons $h\nu = 7940$ eV¹².

The spectral weights of RuO₂ and Ru nanosheets increase as a function of the number of layers. In Fig. 2(c), we compare the valence band spectrum with the band structure calculation of bulk Ru metal obtained by using the WIEN2K package¹⁰. The observed structures in spectra are basically consistent with the band structure calculation. Meanwhile, for RuO₂ nanosheets (1, ~6, and ~9 L), the spectral intensities around -1.5 eV and from -4 eV to -8 eV can be seen in Fig. 2(a). These features derive from the Ru *4d* band and the O *2p* band hybridized with the Ru *4d* states, respectively. Furthermore, the spectral weight at E_F of RuO₂ nanosheets is suppressed in contrast to that of the

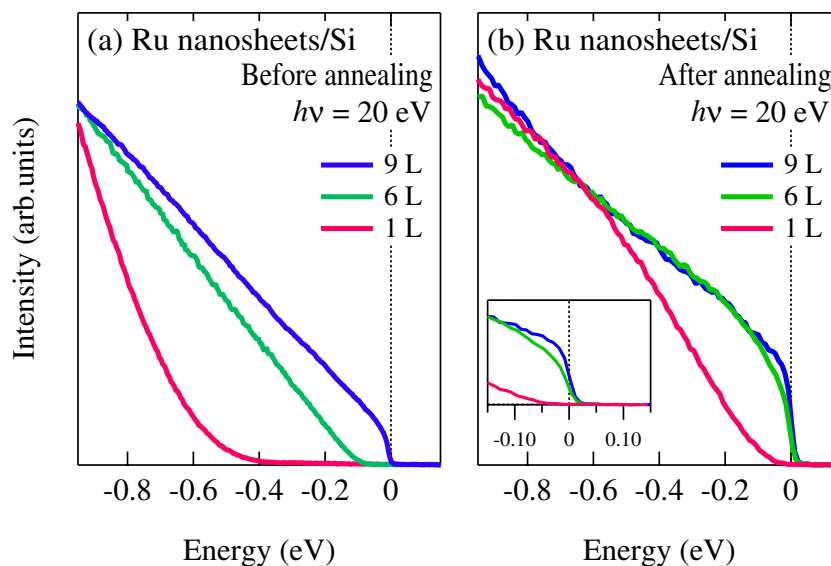


Figure 3. Near- E_F photoemission spectra of Ru nanosheets (1, ~6, and ~9 L) taken at $h\nu = 20$ eV (a) before annealing and (b) after annealing. Inset shows an enlarged view close to E_F . The data were obtained at $T = 28$ K.

thick-layered Ru nanosheets. Thus, the spectral difference between the RuO_2 and Ru nanosheets indicates that the Ru nanosheets are successfully elaborated from the RuO_2 nanosheets by the hydrogen reduction method.

In order to discuss the conductivity from the electronic structure near E_F , we performed the high resolution ultraviolet photoemission spectroscopy. Since the ultraviolet photoemission spectroscopy is the surface sensitive probe ($\lambda \sim 1.0$ nm)¹², we heated the Ru nanosheets up to 300 °C for 15–30 min to obtain the clean surface. Figure 3 shows the number-of-layers dependence of the near- E_F photoemission spectra before and after annealing. The near- E_F photoemission spectra before annealing exhibit the absence of the spectral weight at E_F even in the thick Ru nanosheets (~9 L), suggesting the contamination of the sample surfaces. After annealing, we observed the sharp Fermi cutoff in the spectrum of the thick Ru nanosheets (~9 L) and confirmed that the clean surfaces are obtained by annealing. However, the spectral weight at E_F of the mono-layered Ru nanosheets (1 L) is completely suppressed, indicating the non-metallic behavior as shown in the inset of Fig. 3(b). Interestingly, the spectral weight close to E_F for the thick Ru nanosheets of ~6 L diminishes in contrast to that of ~9 L.

In Fig. 4, the number of layers dependence of the photoemission spectra for Ru nanosheets (1, ~6, and ~9 L) are taken at $h\nu = 800$ eV. The samples were annealed to obtain the clean surface as the same processing in Fig. 3. Figure 4(a) shows the Ru 3 d core-level photoemission spectra of the mono- and few-layered Ru nanosheets (1, ~6, and ~9 L). Note that the C 1 s signal is completely absent in ~9 L sample, which indicates that clean surface was obtained by annealing process. On the other hand, the intensity of C 1 s starts to be observed from ~6 L and the intensity ratio of C 1 s to Ru 3 d core-levels increases in going from ~6 L to 1 L. This trend can be seen in the Si 2 $p/2 s$ of the substrate and the O 2 p signals (see Supplementary Fig. S1). These suggest that the C 1 s feature derives from the cationic coblock polyvinyl alcohol and polyvinyl amine polymers^{7,9} which mainly exist in between Ru nanosheets and Si substrate. Actually, the thickness of ~0.72 nm for 1 L is smaller than the escape depth $\lambda = 1.22$ nm for $h\nu = 800$ eV, consistent with the observation of the remarkable intensity of C 1 s in 1 L. In contrast, the thickness of ~4.32 nm for ~6 L is larger than λ and is correspond to $3\lambda - 4\lambda$ ($\lambda = 1.22$ nm for $h\nu = 800$ eV), which explains the small intensity of C 1 s in ~6 L.

Figure 4(b) shows an enlarged view of the Ru 3 $d_{5/2}$ core-levels. The peak positions of Ru 3 $d_{5/2}$ core-level shift toward higher binding energy with decreasing the number of layers. This behavior is also observed in the previous photoemission study of the Ru nanosheets⁹. The observed shift of the Ru 3 d core-levels from ~9 L to 1 L results from the reduction of the screening effect corresponding to the number of conduction electrons. Indeed, the spectral weight near E_F decreases in going from ~9 L to 1 L and that of the mono-layered Ru nanosheets shows the insulating gap as shown in Fig. 4(c). Here, it should be noted that the peak width of Ru 3 $d_{5/2}$ core-level becomes broad in going from ~9 L to 1 L. The Ru 3 d core-level broadening is probably due to the enhancement of disordered effect, which is reported in many alloys system such as $\text{Cu}_{1-x}\text{Pd}_x$, $\text{Cu}_{1-x}\text{Pt}_x$, and $\text{Pd}_{1-x}\text{Ag}_x$ ^{13–17}. Another possibility is that the increase of the Coulomb interaction induces the core-level broadening proposed by Davis and Feldkamp^{18,19}.

Figure 5 shows the symmetrized near- E_F photoemission spectra of the Ru nanosheets (1, ~6, and ~9 L) taken at $h\nu = 20$ eV and 800 eV in order to visualize the spectral density of states near E_F . The spectral density of states (DOS) of the mono-layer (1 L) and the thick layers (~6 L) depletes as it approaches E_F in contrast to that of ~9 L. The spectral DOS at E_F is completely suppressed in the mono-layered Ru nanosheets (1 L), while that of $N = 6$ L shows the cusp-like shape. These indicate the metal-insulator transition according to the thickness of Ru nanosheets. To address the mechanism of the metal-insulator transition of the Ru nanosheets, we simulate our data taken at $h\nu = 20$ eV using a power law $g(\varepsilon) \propto |\varepsilon - \varepsilon_F|^\alpha$ convoluted with the energy resolution 19 meV. The spectral DOS near E_F are well reproduced using the power factor $\alpha = 0.53$ for 6 L and 1.28 for 1 L as indicated the solid curves in the insets of Fig. 5(c,d). In Fig. 5(c,d), we rescale the energy axis as a function of $\alpha = 0.53$ and 1.28.

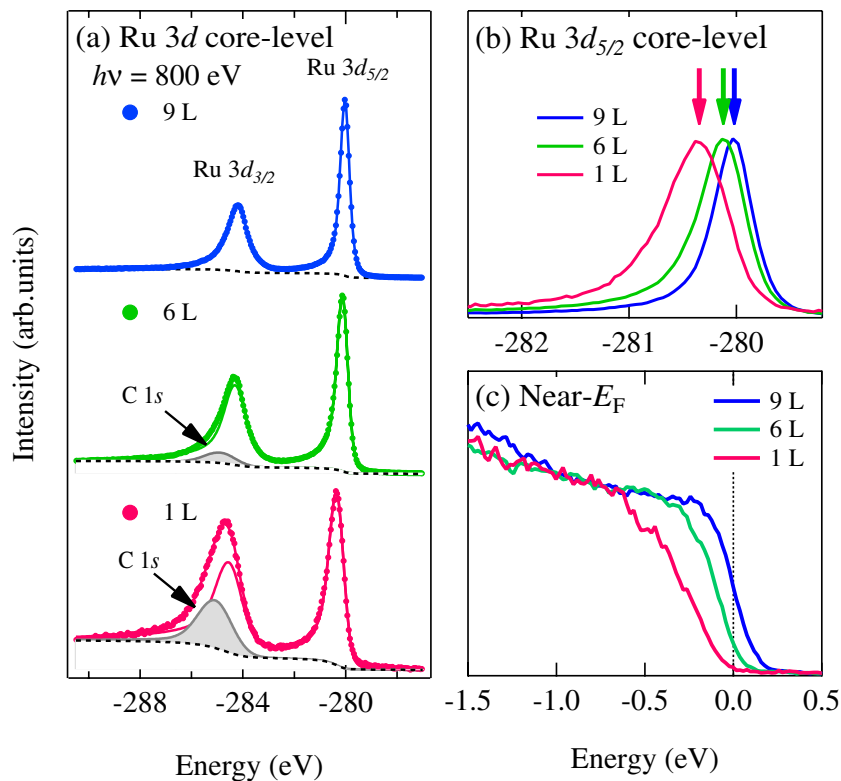


Figure 4. (a) Ru 3d core-level spectra and (b) its enlarged plot of Ru nanosheets (1, ~6, and ~9 L). The photoemission intensity is normalized by the Ru 3d_{5/2} peak intensity. (c) Near- E_F spectra of Ru nanosheets (1, ~6, and ~9 L). The spectra were taken at $h\nu = 800$ eV and $T = 15$ K. The samples were annealed *in situ* to obtain the clean surface.

The power factor $\alpha = 0.53$ of ~6 L is comparable to a singularity of $\alpha = 0.5$, which is estimated to consider the electron-electron interaction in three-dimensional disordered metals²⁰ such as $\text{Ge}_{1-x}\text{Au}_x$ ²¹. On the other hand, the energy dependence $\alpha = 1.28$ in the mono-layered Ru nanosheets is close to $\alpha = 1$. The power law with the exponent $\alpha = 1$ indicates a soft Coulomb gap due to the disorder and the long-range Coulomb interaction, which is predicted in the 2-dimensional insulator by Efros and Shklovskii²². Therefore, our data suggest the transition from the metallic state of ~9 L to the 2-dimensional insulating state with the soft Coulomb gap of 1 L through the disordered 3-dimensional metallic state of ~6 L.

Here, we consider two main possibilities for the deviation from the power factor 1.0 to 1.28 in the mono-layered Ru nanosheets. On the basis of Efros-Shuklovskii theory, the spectral weight at E_F vanishes and the spectral weight near E_F follows the power law with the exponent $\alpha = 1.0$ for the 2 dimensional system²². In the numerical calculation including the disorder effect and Coulomb interaction, the spectral weight near E_F is described by the power law with $\alpha = 1.23$. Moreover, the Coulomb gap is filled at finite temperature²⁴ In any cases, the power factor α can be larger than 1.0. Alternatively, the deviation comes from the overlap region between the mono-layered Ru nanosheets. The AFM image of the mono-layered Ru nanosheets exhibits the overlap region between the Ru nanosheets. Since the electronic structure in the overlap region is not the 2-dimensional but the 3-dimensional, the power factor α would deviate from 1.0. Actually, we estimated the distribution of the mono-layered region is 83.8% and that of the overlap region is 16.2%. On the basis of the Efros-Shuklovskii theory, the power factor α should be 2.0 for the 3-dimensional system. Considering the sum of the power factor α for each regions, the power factor α can be estimated $\alpha = 1.16$.

Although the origin of enhancement of the disorder effects in ~6 and 1 L is still covered, the cusp-like spectral DOS near E_F is observed in ~6 L, which is a peculiar feature in the disordered metals. The increase of the disorder effect may induce the Ru 3d core-level broadening as mentioned in Fig. 4. In addition to the disorder effect, the band width is reduced with decreasing the dimensionality. The Ru - Ru distance also extends from ~6 L to 1 L reported in the in-plane x-ray diffraction studies⁹. The resultant reduction of the band width would drive the enhancement of the effective Coulomb interaction in the mono-layered Ru nanosheets. Therefore, the disorder effect observed in ~6 L is more prominent in the mono-layered Ru nanosheets and the electron-electron correlation increases due to the band width narrowing from ~6 L to 1 L. In consequence, the interplay between the disorder and the Coulomb repulsion would form the soft Coulomb gap and the mono-layered Ru nanosheets become insulator. Our results suggest that the electric conductivity depending on the disorder and Coulomb interaction can be controlled by the number of stacking layers. Thus, the tunable electric conductivity using the Ru nanosheets will lead to the design of the multi-level resistance states for the electronic devices such as non-volatile storage devices. Here, the nanosheets

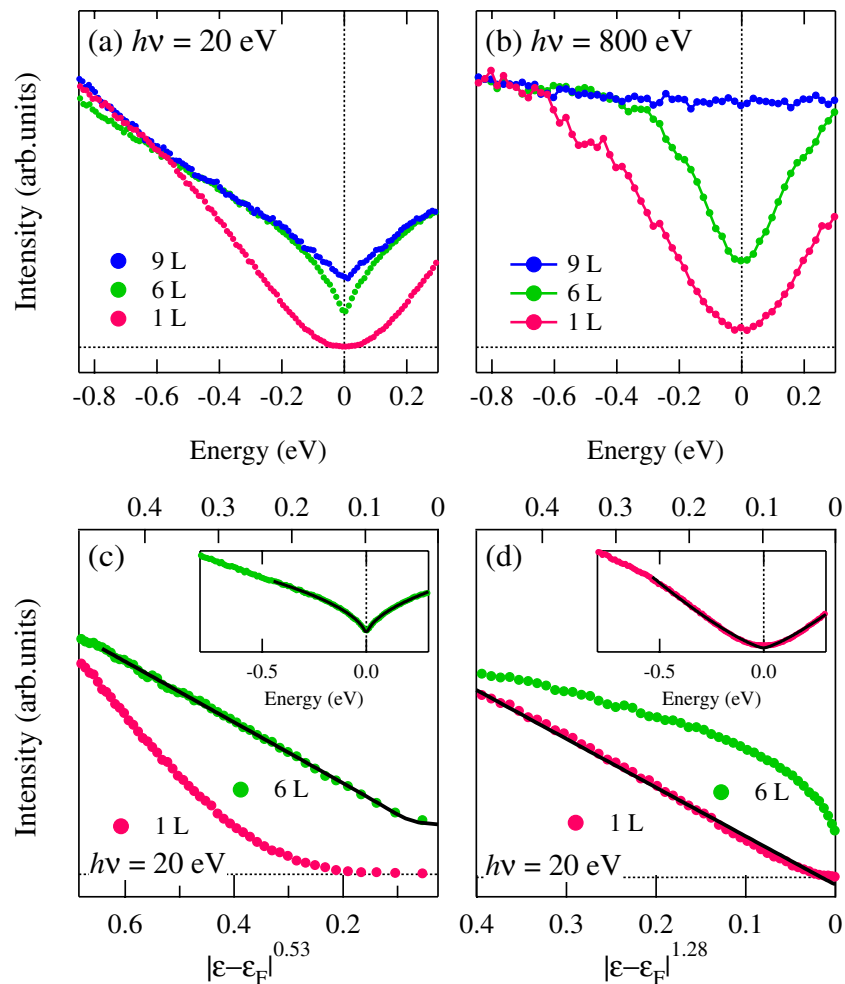


Figure 5. Symmetrized photoemission spectra of Ru nanosheets (1, ~6, and ~9 L) for (a) $h\nu = 20$ eV and (b) 800 eV. The data were taken at $T = 28$ K and $T = 15$ K, respectively. The samples were annealed *in situ* to obtain the clean surface. Symmetrized spectra in (a) are replotted as a function of (c) $|\epsilon - \epsilon_F|^{0.53}$ and (d) $|\epsilon - \epsilon_F|^{1.28}$. The insets indicate the symmetrized spectra and the fitted results. The solid curves represent the fitted curves.

in the present study have statistical dispersion of the number of layers. To further verify the precise dependence of the power factor on the number of layers and the critical thickness for the metal to insulator transition, it would be desirable to synthesize Ru nanosheets with more accurate thickness in future studies.

Conclusion

In summary, we have performed the photoemission spectroscopy of the mono-layered and few-layered Ru nanosheets (1, ~6, and ~9 L) on Si substrate in order to reveal the electronic structure depending on the thickness of Ru nanosheets. The spectral DOS near E_F of 1 L and ~6 L depletes as it approaches E_F , while that of ~9 L shows the clear Fermi cutoff. These are consistent with the chemical shifts of Ru 3 *d* core-level spectra. To verify the origin of the spectral weight suppression near E_F of ~6 L and 1 L, we reproduced the spectral DOS by using the power law. The power factor α increases in going from ~6 L to 1 L, indicating the enhancement of the disorder effect. We found that the transition from the metallic state of ~9 L to the 2-dimensional insulating state with the soft Coulomb gap of 1 L through the disordered 3-dimensional metallic state of 6 L.

Received: 24 June 2019; Accepted: 2 January 2020;

Published online: 30 January 2020

References

- Novoselov, K. S. Electric field effect in atomically thin carbon films. *Sci.* **306**, 666–669, <https://doi.org/10.1126/science.1102896> (2004).
- Vogt, P. *et al.* Silicene: Compelling experimental evidence for graphenelike two-dimensional silicon. *Phys. Rev. Lett.* **108** <https://doi.org/10.1103/physrevlett.108.155501> (2012).
- Fleurence, A. *et al.* Experimental evidence for epitaxial silicene on diboride thin films. *Physical Review Letters* **108** <https://doi.org/10.1103/physrevlett.108.245501> (2012).
- Dávila, M. E., Xian, L., Cahangirov, S., Rubio, A. & Lay, G. L. Germanene: a novel two-dimensional germanium allotrope akin to graphene and silicene. *N. J. Phys.* **16**, 095002, <https://doi.org/10.1088/1367-2630/16/9/095002> (2014).

5. Derivaz, M. *et al.* Continuous germanene layer on al(111). *Nano Lett.* **15**, 2510–2516, <https://doi.org/10.1021/acs.nanolett.5b00085> (2015).
6. Feng, Z. F. *et al.* Epitaxial growth of two-dimensional stanene. *Nat. Mater.* **14**, 1020–1025, <https://doi.org/10.1038/nmat4384> (2015).
7. Fukuda, K. *et al.* Fabrication of ruthenium metal nanosheets via topotactic metallization of exfoliated ruthenate nanosheets. *Inorg. Chem.* **52**, 2280–2282, <https://doi.org/10.1021/ic302720d> (2013).
8. Sato, J., Kato, H., Kimura, M., Fukuda, K. & Sugimoto, W. Conductivity of ruthenate nanosheets prepared via electrostatic self-assembly: Characterization of isolated single nanosheet crystallite to mono- and multilayer electrodes. *Langmuir* **26**, 18049–18054, <https://doi.org/10.1021/la103848f> (2010).
9. Toyoda, S. *et al.* Ligancy-driven controlling of covalency and metallicity in a ruthenium two-dimensional system. *Chem. Mater.* **28**, 5784–5790, <https://doi.org/10.1021/acs.chemmater.6b02019> (2016).
10. Blaha, P. *et al.* An augmented plane wave + local orbitals program for calculating crystal properties.
11. Perdew, J. P., Burke, K. & Ernzerhof, M. Generalized gradient approximation made simple. *Phys. Rev. Lett.* **77**, 3865–3868, <https://doi.org/10.1103/physrevlett.77.3865> (1996).
12. Tanuma, S., Powell, C. J. & Penn, D. R. Calculations of electron inelastic mean free paths. v. data for 14 organic compounds over the 50–2000 eV range. *Surf. Interface Anal.* **21**, 165–176, <https://doi.org/10.1002/sia.740210302> (1994).
13. Cole, R. J., Brooks, N. J. & Weightman, P. Madelung potentials and disorder broadening of core photoemission spectra in random alloys. *Phys. Rev. Lett.* **78**, 3777–3780, <https://doi.org/10.1103/physrevlett.78.3777> (1997).
14. Newton, A., Vaughan, A., Cole, R. & Weightman, P. Disorder broadening of core level photoemission spectra in CuxPt1-x alloys. *J. Electron. Spectrosc. Relat. Phenom.* **107**, 185–191, [https://doi.org/10.1016/s0368-2048\(00\)00100-6](https://doi.org/10.1016/s0368-2048(00)00100-6) (2000).
15. Medicherla, V. & Drube, W. Electronic structure of PdAg(100) ordered surface alloys using synchrotron radiation. *Appl. Surf. Sci.* **256**, 376–379, <https://doi.org/10.1016/j.apsusc.2009.05.043> (2009).
16. Marten, T., Olovsson, W., Simak, S. I. & Abrikosov, I. A. Ab initio study of disorder broadening of core photoemission spectra in randomCu-PdandAg-pdalloys. *Physical Review B* **72** <https://doi.org/10.1103/physrevb.72.054210> (2005).
17. Underwood, T. L., Ackland, G. J. & Cole, R. J. Probing atomic environments in alloys by electron spectroscopy. *Physical Review B* **90** <https://doi.org/10.1103/physrevb.90.014201> (2014).
18. Davis, L. C. & Feldkamp, L. A. Effect of electron correlations on photoemission from narrow-band metals. *J. Appl. Phys.* **50**, 1944–1949, <https://doi.org/10.1063/1.327119> (1979).
19. Davis, L. C. Photoemission from transition metals and their compounds. *J. Appl. Phys.* **59**, R25–R64, <https://doi.org/10.1063/1.336323> (1986).
20. Altshuler, B. & Aronov, A. Zero bias anomaly in tunnel resistance and electron–electron interaction. *Solid. State Commun.* **30**, 115–117, [https://doi.org/10.1016/0038-1098\(79\)90967-0](https://doi.org/10.1016/0038-1098(79)90967-0) (1979).
21. McMillan, W. L. & Mochel, J. Electron tunneling experiments on AmorphousGe1-xAux. *Phys. Rev. Lett.* **46**, 556–557, <https://doi.org/10.1103/physrevlett.46.556> (1981).
22. Efros, A. L. & Shklovskii, B. I. Coulomb gap and low temperature conductivity of disordered systems. *J. Phys. C: Solid. State Phys.* **8**, L49–L51, <https://doi.org/10.1088/0022-3719/8/4/003> (1975).
23. Möbius, A., Richter, M. & Dritler, B. Coulomb gap in two- and three-dimensional systems: Simulation results for large samples. *Phys. Rev. B* **45**, 11568–11579, <https://doi.org/10.1103/physrevb.45.11568> (1992).
24. Sarvestani, M., Schreiber, M. & Vojta, T. Coulomb gap at finite temperatures. *Phys. Rev. B* **52**, R3820–R3823, <https://doi.org/10.1103/physrevb.52.r3820> (1995).

Acknowledgements

The authors would like to thank S. Yamamoto, D. Shibata, M. Kawamoto for experimental supports. This work was supported by Grants-in-Aid for Science Research (C) from the Japan Society for the Promotion of Science (16K05445), the Murata Science Foundation, and the Kyoto University Foundation. The synchrotron radiation experiments were performed with the approvals of SPRing-8 (Proposal No.2015B1462, 2017A1406), Hiroshima Synchrotron Radiation Center (Proposal No. 14-A-13), and Photon Factory (proposal No. 2015G704, 2016G196).

Author contributions

D.O., K.K., D.S. performed the photoemission measurements. M.A., H.N., M.T., M.M., K.H., H.K., E.I., A.Y. supported the synchrotron photoemission experiments. M.M. performed the AFM characterization. Y.U., S.T., M.M., K.F. provided the samples. D.O., K.K. analyzed the photoemission data. D.O. and T.Y. wrote the paper. K.F. and T.Y. designed the project. All authors reviewed the manuscript.

Competing interests

The authors declare no competing interests.

Additional information

Supplementary information is available for this paper at <https://doi.org/10.1038/s41598-020-58057-9>.

Correspondence and requests for materials should be addressed to D.O. or T.Y.

Reprints and permissions information is available at www.nature.com/reprints.

Publisher's note Springer Nature remains neutral with regard to jurisdictional claims in published maps and institutional affiliations.



Open Access This article is licensed under a Creative Commons Attribution 4.0 International License, which permits use, sharing, adaptation, distribution and reproduction in any medium or format, as long as you give appropriate credit to the original author(s) and the source, provide a link to the Creative Commons license, and indicate if changes were made. The images or other third party material in this article are included in the article's Creative Commons license, unless indicated otherwise in a credit line to the material. If material is not included in the article's Creative Commons license and your intended use is not permitted by statutory regulation or exceeds the permitted use, you will need to obtain permission directly from the copyright holder. To view a copy of this license, visit <http://creativecommons.org/licenses/by/4.0/>.

© The Author(s) 2020